

Ultra-Light and Scalable Composite Lattice Materials

Christine E. Gregg, Joseph H. Kim, and Kenneth C. Cheung*

Architected lattice materials are some of the stiffest and strongest materials at ultra-light density ($<10 \text{ mg cm}^{-3}$), but scalable manufacturing with high-performance constituent materials remains a challenge that limits their widespread adoption in load-bearing applications. We show mesoscale, ultra-light (5.8 mg cm^{-3}) fiber-reinforced polymer composite lattice structures that are reversibly assembled from building blocks manufactured with a best-practice high-precision, high-repeatability, and high-throughput process: injection molding. Chopped glass fiber-reinforced polymer (polyetherimide) lattice materials produced with this method display absolute stiffness (8.41 MPa) and strength (19 kPa) typically associated with metallic hollow strut microlattices at similar mass density. Additional benefits such as strain recovery, discrete damage repair with recovery of original stiffness and strength, and ease of modeling are demonstrated.

Strong and stiff ultra-light materials are desirable for structural applications where mass strongly influences performance and cost. In particular, mechanical properties such as specific modulus govern the design of aerospace structures with critical dynamic modes.^[1] Theoretical upper bounds predict the possibility of engineering ultra-light materials that achieve stiffness and strength in the regime of conventional solid materials, exceeding the performance of their constituent solid materials for dynamic mode limited applications. There may be revolutionary benefits to infrastructure and transportation technologies if these limits can be approached with scalable manufacturing methods.^[1,2]

Materials can be engineered with ultra-light density as cellular solids by leveraging an open microstructure. Encompassing stochastic foams, lattice materials, many aerogel structures, and natural materials like bone, cork, and honeycomb, cellular materials in general have mechanical behavior that is governed by their microstructural geometry, constituent material, and manufacturing method. Their performance is typically characterized relative to the solid constituent material. Seminal work by Ashby^[3] established that the stiffness of a cellular solid can be described by:

$$E^- = A\bar{\rho}^a \quad (1)$$

where E^- is relative modulus, the modulus of the lattice normalized by the modulus of the constituent solid, and ρ^- is relative density, the density of the lattice normalized by the density of the constituent solid. A and a are constant scaling factors dependent on cellular geometry, and A is additionally dependent on material and manufacturing method. A similar scaling relationship is established for relative strength, the strength of the lattice normalized by constituent material strength:

$$\sigma^- = B\bar{\rho}^b \quad (2)$$

This is only considered valid for brittle elastic materials or the yield strength of elasto-plastic materials. The scaling factors b and B are known to change depending on the relative density regime, as well as lattice geometry, material, and manufacturing method. Geometry effects for both strength and stiffness are governed by whether the lattice is bend or stretch-dominated, commonly indicated by the lattice connectivity,^[4] and by the cross-sectional geometry of the struts. The stiffest and strongest lattices for their weight feature stretch dominated lattice geometry.


Stochastic foams^[5] and aerogels^[6] can be produced in relatively large quantities, but they feature bend-dominated structures that do not meet the mechanical performance of most architected lattice materials. Conversely, though stretch-dominated architected lattices are some of the lightest and stiffest materials to date,^[7] wide-scale implementation has been limited by manufacturing scalability challenges. Printing,^[8–10] templating,^[7,11] and photolithography methods,^[7,12] commonly used to manufacture architected lattice materials, are intrinsically size limited. Though some roll-to-roll manufacturing strategies have been proposed for metallic lattice sandwich structures,^[13] comparable scalable manufacturing for three-dimensional lattices has yet to be developed.

Manufacturing of cellular materials by assembly of discrete building blocks, each manufactured with conventional best practices, may overcome such limitations. Cheung and Gershenfeld^[14] demonstrated assembled ultra-light engineered cellular materials with specific modulus governed by linear scaling, and others have showed similar performance at lightweight material mass densities using similar methods.^[15–17]

Using this building block approach, we show that near-ideal stiffness and strength behavior can be achieved at ultra-light mass density, using industrial mass production processes. We assemble a lattice using injection-molded thermoplastic

Dr. K. C. Cheung, J. H. Kim
NASA Ames Research Center
Moffett Field
CA 94035, USA
E-mail: kenny@nasa.gov

C. E. Gregg
Department of Mechanical Engineering
University of California Berkeley
Berkeley, CA 94720, USA

 The ORCID identification number(s) for the author(s) of this article can be found under <https://doi.org/10.1002/adem.201800213>.

DOI: 10.1002/adem.201800213

building blocks, produced very quickly (17 s per building block) and inexpensively (0.01–0.03 USD per cubic centimeter). The result is an ultra-light lattice material that, despite theoretical material and geometric disadvantages, displays stiffness and strength behavior in the regime of state of the art metallic and ceramic microlattices. This strategy leverages well-characterized manufacturing processes that can utilize a wide variety of materials. In addition, mass manufacturability, high fidelity behavior prediction with low resolution modeling, and discrete repairability may enable practical wide-scale implementation.

Cuboctahedral lattices were assembled from injection molded octahedral unit cells termed voxels (**Figure 1**). Two different constituent materials were tested: Ultem 2200 (20% glass fiber reinforced polyetherimide), and stiffer, more brittle RTP 2187 (40% carbon fiber reinforced polyetherimide). Significant alignment of the chopped fibers within the strut, caused by shear during the injection molding process, was observed in both materials (**Figure 1f**). In the case of Ultem 2200, this produced higher effective strength and stiffness than manufacturer data sheet values. Voxels had a pitch, or unit cell length, of 3 in, and a strut cross-sectional area of 2.63×10^{-3} square inches (**Figure S1**). Stainless steel size 0–80 bolts and nuts torqued to specification (16 in-oz) provided reversible and repeatable node connections.

Various specimen sizes were tested, each forming a cube with n unit cells per side (total of n^3 voxels per specimen). Converged continuum behavior for modulus was reached by $n=4$ (**Figure S6**). Symmetric linear elastic behavior in tension and

compression was observed for Ultem 2200 lattices, with low hysteresis during cyclic loading (**Figure 2a**). Upon initiation of strut buckling, a non-linear elastic region is observed that resembles a bulk yield-like behavior, though with no associated plastic strain (**Figure 2b**). Upon unloading, strain and modulus are almost fully recovered (99%). The first reloading into the non-linear region (35% of average break strain) shows a small reduction in the proportionality limit (to 95% of original), which we attribute to small strain setting in the node connections affecting buckling bias. Considerable permanent change in material behavior is only observed after strut breaking initiates.

An ABAQUS FEA model showed outstanding fidelity in the linear-elastic region using a relatively small mesh size, attributed to the discrete nature of the material as a network of beams (**Figure 3**). Modeling results for an $n=4$ Ultem 2200 lattice predicted a lattice stiffness of 2.71 MPa, which differs by less than 5% from average measured experimental values for tension (2.61 MPa) and compression (2.60 MPa). Discrepancy in predicted yield behavior is attributed to the necessary rectangular approximation of the real kite-shaped strut profile, resulting in small differences in second moment of area and the buckling behavior of the beams.

While linear elastic behavior was symmetric in tension and compression, post-buckling behavior of Ultem 2200 lattices varied in compression and tension (**Figure 3**) and initiated at a lower average stress in compression (10.4 KPa vs. 6.28 KPa). When in tension, struts in the plane normal to loading are in compression and eventually buckle (**Figure 3a**). After these struts

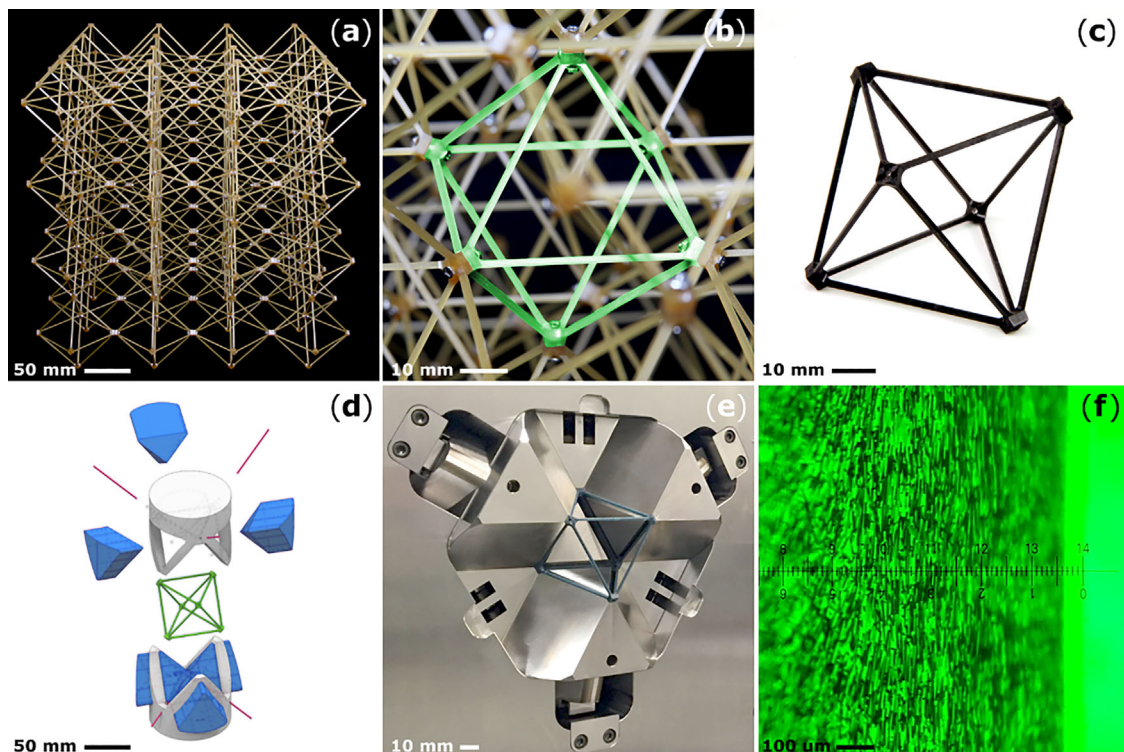


Figure 1. a) An assembled cuboctahedral lattice specimen, made from b) Ultem 2200 (20% glass fiber reinforced polyetherimide) octahedral unit cells (highlighted), termed voxels. c) A single monolithic RTP 2187 (40% carbon fiber reinforced polyetherimide) injection molded voxel. d) Exploded view of the injection mold. e) Picture of the mold surface. f) Micrograph showing fiber alignment within the RTP 2187 injection molded strut.

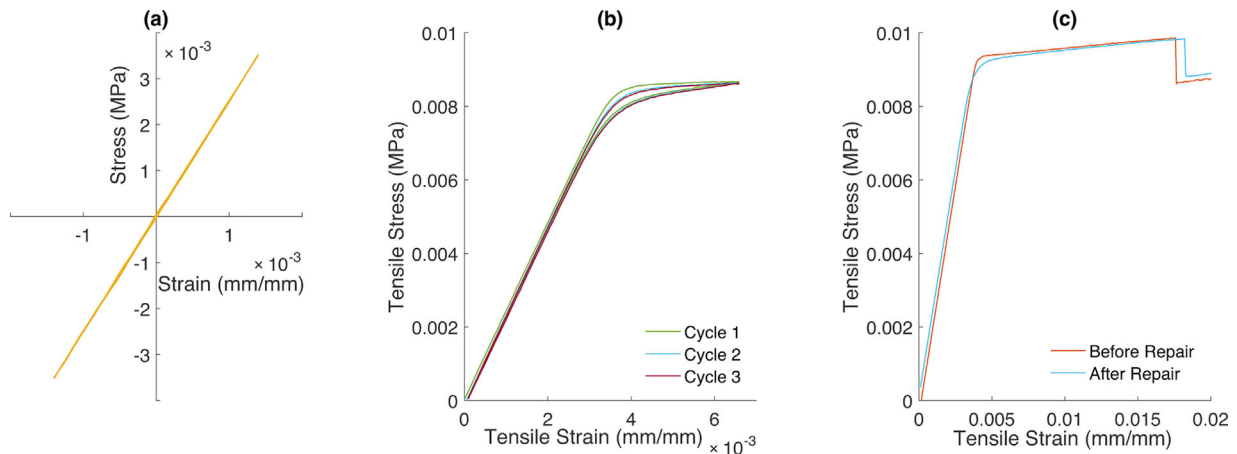


Figure 2. a) Cyclic loading of an $n = 2$ Ultem 2200 lattice in tension and compression in the linear-elastic regime demonstrating symmetric behavior in tension and compression and low hysteresis. b) Loading (top three curves) and unloading (bottom three curves) of an $n = 2$ Ultem 2200 lattice from the non-linear elastic region shows an initial reset of the proportionality limit (95% of original) attributed to buckling bias and small strain set in the nodes. c) Stress–strain response of an $n = 2$ Ultem 2200 lattice assembly before and after repair via voxel replacement, each loaded until a single strut failure.

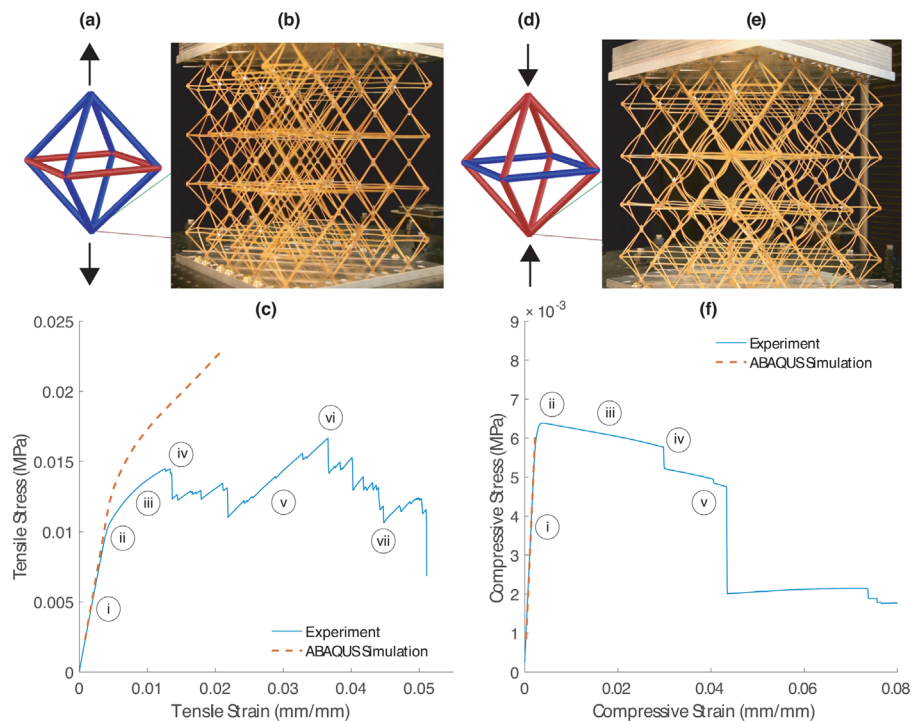


Figure 3. a) Diagram showing which struts are in compression (red) and which struts are in tension (blue) under global tensile loading. b) Picture showing deformation modes of an $n = 4$ Ultem 2200 lattice under tensile loading. c) Representative tensile response of an $n = 4$ Ultem2200 lattice assembly and associated simulation results. Distinct behavioral regions of the experimental curve can be seen in (i) linear elastic behavior; (ii) initiation of strut buckling and non-linear elastic regime; (iii) hardening caused by alignment of struts with load direction due to buckling deformation; (iv) first strut failure; (v) second hardening regime caused by continued strut alignment with load; (vi) ultimate strength; and (vii) final degradation with continued strut failure. d) Diagram showing which struts are in compression (red) and which struts are in tension (blue) under global compressive loading. e) Picture showing deformation modes of an $n = 4$ Ultem 2200 lattice under compressive loading. f) Representative compressive response of an $n = 4$ Ultem2200 lattice assembly and simulation results. Distinct behavioral regions of the experimental curve can be seen in (i) linear elastic response; (ii) initiation of strut buckling and non-linear elastic behavior; (iii) softening as buckling causes strut misalignment with load; (iv) first strut failure; and (v) catastrophic strut failure and continued degradation.

buckle, the material exhibits a bulk hardening effect as deformation modes cause struts originally in tension to further align with the load direction. A similar mechanism is known in stochastic foams^[18] and was recently described for two-dimensional architected lattice geometries.^[19] After the first few compressed struts break, further bulk hardening is observed as load alignment continues. Eventually, aligned struts begin to break, and final degradation occurs. The opposite mechanism operated in compression, where struts in the plane normal to loading were in tension (Figure 3d). Buckling of struts outside of this plane resulted in increased beam-bending dominated behavior and softening after the bulk non-linear transition, before breakage led to continued material failure. Because of the more brittle nature of the RTP 2187 lattices, no post-damage hardening was observed (Figure S3 and S4). We attribute this to insufficient ability to achieve load alignment without breaking.

The assembled lattices demonstrated outstanding behavior upon discrete repair (the replacement of a broken voxel with a new voxel). Figure 2c shows the stress–strain curve of an $n = 2$ Ultem 2200 sample loaded until a single strut failed. It was then unloaded and the single broken voxel was replaced using the reversible bolted connection. Reloading showed that the repaired structure maintained stiffness equivalent to the original sample (2.52 vs. 2.48 MPa), with a small decrease in yield strength (retains 95% of original strength), attributed to strain setting mechanisms discussed previously.

An Ashby chart of relative modulus vs. relative density for ultra-light materials demonstrates the importance of manufacturing process on lattice performance. The relative modulus can be thought of as a quantitative measure for how efficiently the manufacturing method and geometry combine to utilize the available performance of a material. Injection molded lattices achieve the same relative stiffness regime as state of the art metallic hollow microlattices (Figure 4), despite a 20% mass penalty from nut and bolt hardware and less efficient solid struts.^[20] Both types of injection molded cuboct lattice outperform an assembled uni-directional CFRP cuboct lattice of higher relative density.^[14] Since they use the same cellular geometry, this difference can be primarily attributed to the manufacturing. The same behavior is observed in absolute modulus (Figure 4b), where injection molded lattices are competitive with metallic and ceramic microlattices.

Injection molded lattices achieve the same regime of relative strength as other architected lattice materials (Figure 5). The difference between the RTP 2187 and Ultem 2200 relative strength is attributed to their differing degrees of ductility and strut buckling strength (per modulus), full discussion of which is available in the Supplementary Information.

By demonstrating injection molded lattices, we show that selecting materials for manufacturability with traditional, high-precision processes can create lattices with state of the art performance while offering many additional benefits. Assembly from building blocks that took seconds to make and an unconstrained build envelope offer true mass manufacturability, in addition to discrete reparability. This strategy may enable production of complex assemblies at mass production scale that achieve high-performance ultra-light material properties. The specific mechanical performance advantages are particularly relevant to applications with critical dynamic modes, such as

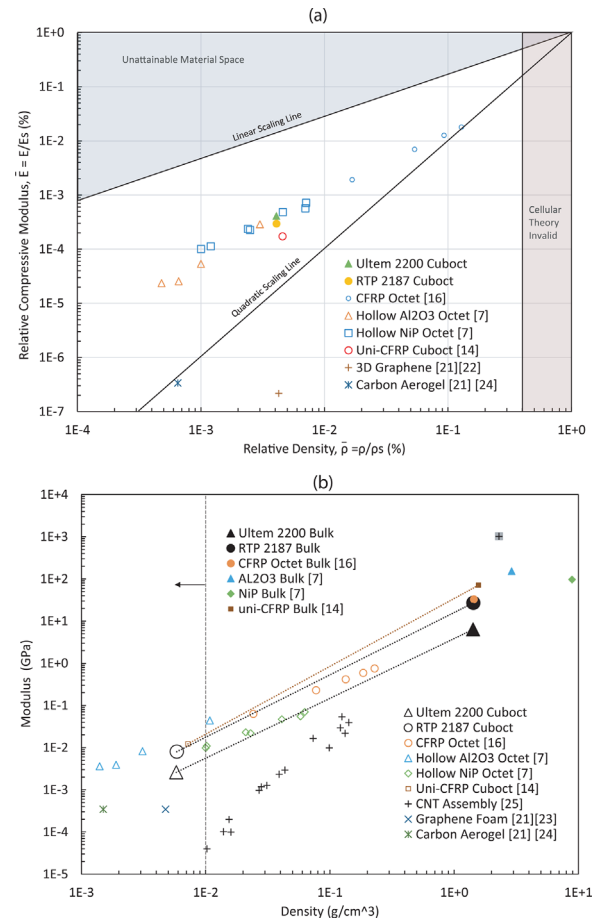


Figure 4. a) A comparison of ultra-light materials shows the high relative performance of injection molded lattices ($n = 4$). b) Injection molded lattices achieve the same absolute performance regime as ceramic and metallic hollow microlattices. Dotted lines compare the scaling of injection molded cuboct lattice with an assembled unidirectional CFRP cuboct lattice,^[14] demonstrating how higher relative performance of RTP 2187 cuboct causes the convergence of performance. Values from this work were normalized with the average measured strut stiffness of the respective material.

aerospace structures, with performance metrics that scale with the square or cube root of stiffness per mass density.^[1] Building block based assembly provides opportunities spanning the material lifecycle, potentially streamlining design, analysis, manufacturing, and servicing to fully realize the potential of lattice materials in transformative structural applications.

2. Experimental Section

Manufacturing: Octahedral voxels were produced as monolithic thermoplastic injection molded parts, using custom designed tooling. This tooling was commercially manufactured from hardened steel for operation in a commercial press, with conventional fluid heating according to temperature limits specified for the compounds used (by the compound manufacturers). The complex geometry was achieved using twelve slides, with six larger triangular slides (Figure 1d, blue) forming

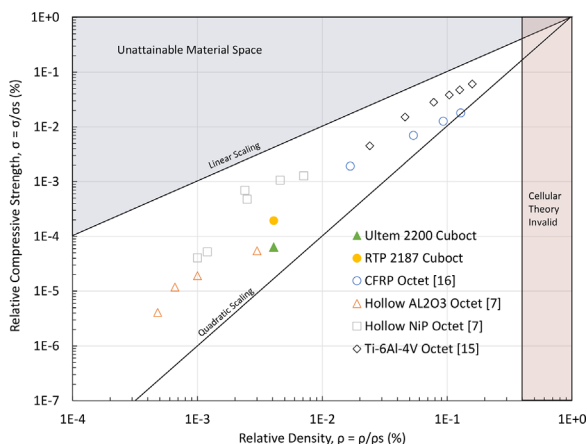


Figure 5. Injection Molded lattices achieve the same regime of behavior as other ultra-light lattices. Values from this work were normalized with yield strength of the weakest strut in a voxel.

shutoffs against each other and the two mold halves in groups of four to form struts composing each triangular face of the voxel. Six smaller cylindrical slides (Figure 1d, magenta) formed the fastener holes in each node. Tolerances for the tooling surfaces were specified to less than $25\ \mu\text{m}$, with the mold cavity (Figure 1e) scaled according to the coefficient of thermal expansion of the fiber reinforced compound. Complete process cycle time was approximately 17 s per part. Voxel struts had a kite shaped strut cross-section detailed in Figure S1. To characterize the mechanical behavior of each material, struts were extracted from each voxel type and tensile tested at a strain rate approximating that seen in the assembled lattices ($0.0002\ \text{mm/mm/s}$). Figure S2 shows characteristic stress-strain curves for both materials. Because of the small length scale characteristic of the strut cross section, both materials showed significant fiber alignment within the struts due to shear during injection molding (Figure 1f). Additionally, the stiffness of the strut varied depending upon the presence of a knit line from the injection molding design. Half of the struts in each voxel have a knit line in the center of the strut. Full discussion and results of material characterization can be found in the Supplementary Information, where it was shown that the average stiffness of knit line struts and non-knit line struts effectively characterized overall lattice behavior. The relative density of each lattice was measured to include the mass of the bolted connection.

Testing: Various sizes of cubic specimens ($n = 1, 2, 3, 4$) were assembled from Ultem 2200 injection molded voxels. Each size was tested in triplicate in both tension and compression, first cyclically loaded in the linear-elastic regime, then loaded until failure. The top and bottom surface nodes of each lattice block were bolted to aluminum fixture plates, which were then bolted to an Instron 5982 testing machine. Each specimen size was loaded at a constant strain rate of $0.00066\ \text{mm/mm/s}$. To characterize a repaired $n = 2$ lattice, the lattice was loaded first in tension using previously described test parameters until a single strut failure. The lattice was then unloaded, the broken voxel was replaced, and the repaired lattice reloaded in tension. The same testing procedure was used for RTP 2187 lattices, but only $n = 4$

specimens were tested in tension and compression (Figure S3 and S4). Full results for Ultem 2200 and RTP 2187 lattices are tabulated in Supplementary Materials.

Simulation: Compression and tension behavior of the Ultem 2200 lattices were simulated using ABAQUS, using the non-linear geometry option to capture large strains. Each voxel contained six nodes and twelve edges, each edge subdivided into four B31 elements. A rectangular element cross-section ($0.0611\ \text{in}$ by $0.0429\ \text{in}$) was used, selected to equal the second moment of area about the minor kite axis of the actual strut cross section, as well as the total cross sectional area. To increase model fidelity, the thickness of the node connections was modeled using a single thicker beam matched to the size of the injection molded node (Figure S7). The average modulus of $6.25\ \text{GPa}$ measured from strut testing and a 0.38 Poisson ratio (data sheet value) were used. An ENCASTRE boundary condition was applied to the bottom nodes, and the top nodes were connected to S4R shell elements and constrained to the same z displacement. Forces in the z direction were applied to each node.

Acknowledgements

The authors gratefully acknowledge support from the NASA Space Technologies Research Fellowship (grant no. NXX16AM65H), as well as the NASA ARMD Convergent Aerospace Solutions and NASA STMD Game Changing Development programs. We also thank Daniel Cellucci, Olivia Formoso, Benjamin Jenett, Sean Swei, Greenfield Trinh, and Khanh Trinh for critical discussions and research assistance.

Conflict of Interest

Patent applications have been filed for the manufacturing of reversibly assembled cellular composite materials. The authors declare no other conflicts of interest.

Keywords

cellular solid, lattice, ultra-light

Final Version: April 13, 2018
Received: March 1, 2018
Published online: May 14, 2018

- [1] S. M. Arnold, D. Cebon, M. Ashby, *Introd. to Aerosp. Mater.* **2012**, 569. NASA/TM—2012-217411.
- [2] L. Valdevit, A. J. Jacobsen, J. R. Greer, W. B. Carter, *J. Am. Ceram. Soc.* **2011**, 94, s15.
- [3] M. F. Ashby, *Metall. Trans. A* **1983**, 14, 1755.
- [4] V. S. Deshpande, M. F. Ashby, N. A. Fleck, *Acta Mater.* **2001**, 49, 1035.
- [5] B. Jiang, C. He, N. Zhao, P. Nash, C. Shi, Z. Wang, *Sci. Rep.* **2015**, 5, 13825.
- [6] H. Hu, Z. Zhao, W. Wan, Y. Gogotsi, J. Qiu, *Adv. Mater.* **2013**, 25, 2219.
- [7] X. Zheng, H. Lee, T. H. Weisgraber, M. Shusteff, J. Deotte, E. B. Duoss, J. D. Kuntz, M. M. Biener, Q. Ge, J. A. Jackson, S. O. Kucheyev, N. X. Fang, C. M. Spadaccini, *Science* **2014**, 344, 1373.

- [8] C. Zhu, T. Y. J. Han, E. B. Duoss, A. M. Golobic, J. D. Kuntz, C. M. Spadaccini, M. A. Worsley, *Nat. Commun.* **2015**, 6, 1.
- [9] A. Maiti, W. Small, J. P. Lewicki, T. H. Weisgraber, E. B. Duoss, S. C. Chinn, M. A. Pearson, C. M. Spadaccini, R. S. Maxwell, T. S. Wilson, *Sci. Rep.* **2016**, 6, 24871.
- [10] B. G. Compton, J. A. Lewis, *Adv. Mater.* **2014**, 26, 5930.
- [11] T. A. Schaedler, A. J. Jacobsen, A. Torrents, A. E. Sorensen, J. Lian, J. R. Greer, L. Valdevit, W. B. Carter, *Science* **2011**, 334, 962.
- [12] L. R. Meza, S. Das, J. R. Greer, *Science* **2014**, 345, 1322.
- [13] M. G. Rashed, M. Ashraf, R. A. W. Mines, P. J. Hazell, *Mater. Des.* **2016**, 95, 518.
- [14] K. C. Cheung, N. Gershenfeld, *Science* **2013**, 341, 1219.
- [15] L. Dong, V. Deshpande, H. Wadley, *Int. J. Solids Struct.* **2015**, 60, 107.
- [16] L. Dong, H. Wadley, *Compos. Sci. Technol.* **2015**, 119, 26.
- [17] X.-T. Wang, X.-W. Li, L. Ma, *Mater. Des.* **2016**, 99, 467.
- [18] L. J. Gibson, M. F. Ashby, *Cellular Solids: Structure and Properties*, Cambridge University Press, New York, **1997**.
- [19] H. C. Tankasala, V. S. Deshpande, N. A. Fleck, *J. Mech. Phys. Solids* **2017**, 109, 307.
- [20] D. T. Queheillalt, H. N. G. Wadley, *Acta Mater.* **2005**, 53, 303.
- [21] Z. Qin, G. S. Jung, M. J. Kang, M. J. Buehler, *Sci. Adv.* **2017**, 3, 1.
- [22] X. Xie, Y. Zhou, H. Bi, K. Yin, S. Wan, L. Sun, *Sci. Rep.* **2013**, 3, 1.
- [23] A. Nieto, B. Boesl, A. Agarwal, *Carbon N. Y.* **2015**, 85, 299.
- [24] H. Sun, Z. Xu, C. Gao, *Adv. Mater.* **2013**, 25, 2554.
- [25] M. A. Worsley, S. O. Kucheyev, J. H. Satcher, A. V. Hamza, T. F. Baumann, *Appl. Phys. Lett.* **2009**, 94, 1.